







Near Real-Time Monitoring of Muddy Intertidal Zones Based on Spatiotemporal Fusion of Optical Satellites Data

Yan Gu , Jianchun Chen , *Graduate Student Member, IEEE*, Ziyao Chen , Mingliang Li , Shibing Zhu ,
and Ya Ping Wang 

Abstract—The investigation of the evolution of intertidal zones is a significant and extensively discussed subject in estuary and coastal research, both nationally and internationally. Recent advances in real-time global satellite products, such as GOCI, provide a potential approach for monitoring intertidal zones by utilizing waterline inversion based on spatial distribution processes. While these products offer the potential for monitoring intertidal zones through waterline inversion based on spatial distribution processes, they often suffer from coarse spatial resolution that smooths critical spatial heterogeneity. To overcome this limitation, a flexible spatiotemporal fusion model was employed to generate hourly time-series images with a spatial resolution of 10 m. This was achieved by combining Sentinel-2 satellite data (10 m spatial resolution; five-day revisit frequency) and GOCI-II data (500 m spatial resolution; 1-h revisit frequency). The resulting fusion images were used to construct an intertidal pseudodigital elevation model (DEM) by extracting waterlines and incorporating tidal-level information. The accuracy of the DEM was validated using surveyed real-time kinematic and drone data, with a root-mean-square error of 0.28 m. The analysis of the annual accretion and erosion evolution in the intertidal zone for the year 2023 revealed significant erosion in the central part of the zone, with a maximum erosion depth of 1 m at the bottom. This study contributes to the understanding of the response processes and mechanisms of the intertidal zone to natural and human disturbances, thus supporting coastal planning projects related to the intertidal zone.

Index Terms—Environment monitoring, flexible spatiotemporal data fusion (FSDAF), GOCI-II, muddy intertidal zone, optical satellites, spatiotemporal fusion, terrain inversion.

Manuscript received 28 August 2023; revised 9 November 2023; accepted 30 November 2023. Date of publication 5 December 2023; date of current version 18 December 2023. This work was supported in part by the National Natural Science Foundation of China under Grant 41801006, in part by the Jiangsu Special Program for Science and Technology Innovation under Grant JSZRHYKJ202106, and in part by Jiangsu Provincial Department of Education under Grant KYCX23_1067. (*Corresponding authors: Yan Gu; Ya Ping Wang.*)

Yan Gu, Jianchun Chen, and Ziyao Chen are with the School of Geography and Biologic Information, Nanjing University of Posts and Telecommunications, Nanjing 210033, China (e-mail: guyan@njupt.edu.cn; 1021173520@njupt.edu.cn; 1022173212@njupt.edu.cn).

Mingliang Li and Shibing Zhu are with the School of Geography and Marine Science, Nanjing University, Nanjing 210033, China (e-mail: 798015501@qq.com; 26585759@qq.com).

Ya Ping Wang is with the State Key Laboratory of Estuarine and Coastal Research, School of Marine Sciences, East China Normal University, Shanghai 200062, China (e-mail: ypwang@nju.edu.cn).

Digital Object Identifier 10.1109/JSTARS.2023.3339339

I. INTRODUCTION

THE intertidal zone refers to the area that is submerged during high tide and exposed during low tide [1]. It is a vital component of wetland systems, playing a critical role in providing a range of ecosystem services. These services include global climate regulation, storm surge protection, natural water purification, and coastal erosion prevention [2]. However, despite its ecological and economic significance, due to human activities and the anticipated future rise in sea levels, the intertidal zone is highly susceptible to damage. With the development of the economy, the excessive exploitation and utilization of intertidal zones have resulted in irreversible consequences for intertidal ecosystem [3], [4]. Furthermore, short-term changes in the topography of the intertidal zone caused by the passage of storm surges have a significant impact on coastal areas [5]. Therefore, monitoring the changes in intertidal zone topography is an important task for coastal planning projects, crucial for a better understanding of intertidal zone system evolution and management [6].

In recent years, the measurement of the intertidal zone has posed a significant challenge [7]. Intertidal topography can only be measured when the intertidal zone is exposed at low tide; traditional measurement techniques, such as control measurement, photogrammetry, and real-time kinematic (RTK) measurement, can be all used for intertidal topographic measurements [8]. However, these techniques have certain limitations, such as high time and financial costs, and can only provide localized data within the study area, unable to obtain large-scale and wide-ranging data on a global scale [9], [10]. Advancements in spatial science, sensor technology, and graphic image processing have led to significant progress in remote sensing technology. This technology now allows for the convenient acquisition of high-resolution remote sensing images within a study area [11], [12]. This development has addressed the limitations of traditional measurement techniques, including time consumption, costs, and limited study areas. As a result, remote sensing technology has become widely used in monitoring the intertidal zone [13], [14], [15]. For instance, Ryu et al. [16] utilized three-dimensional (3-D) images generated from remote sensing data to create a digital surface model for studying and analyzing the intertidal zone; Maiti and Bhattacharya [7] used various time-series remote sensing images to extract the shoreline and

applied the shoreline method to analyze the evolution of intertidal landforms; Letortu et al. [18] employed LiDAR technology and ground-based LiDAR to create a high-resolution digital terrain model (DTM) in coastal areas; Wang et al. [17] used the Google Earth engine (GEE) cloud platform and decision tree algorithm to investigate the evolution of intertidal landforms in China between 1986 and 2016. Fitton et al. [19] used tidal calibration satellite imagery (Sentinel-2) to measure the frequency of water occurrence and processed it within the GEE to create a map of the intertidal zone in the United Kingdom and the Republic of Ireland. Liu et al. [20] have utilized the shoreline method to invert the digital elevation model (DEM) of Dongsha Sandbank in China from 1993 to 2009. However, remote sensing images are affected by a “spatiotemporal contradiction” problem. The high-resolution images have long revisit cycles, resulting in limited availability of waterline data at specific times. The traditional waterline method is actually an average intertidal zone method for years, seasons, and months. It extracts the shoreline within a certain period of time; the obtained data represent the average variation of the intertidal zone during the specified period, which is significantly different from the actual topography. On the other hand, high-temporal-resolution images often suffer from accuracy issues due to their low spatial resolution [21]. To overcome this challenge, remote sensing image fusion technology combines high-temporal and high-spatial-resolution images, enabling the generation of near real-time remote sensing images and resolving the “spatiotemporal contradiction” problem [22].

With the continuous advancement of computer science, technology, and image processing techniques, various algorithms have emerged in the field of spatiotemporal fusion of remote sensing images. These algorithms can be classified into five categories: unmixing-based methods, Bayesian-based methods, learning-based methods, weighted-function-based methods, and mixture-based methods [23]. The multiresolution technique proposed by Wei et al. [24] in 1999 is the first unmixing-based spatiotemporal fusion algorithm, known for its high computational efficiency. However, the unmixing-based fusion method only deals with coarse-resolution images and does not consider the mixed pixel phenomenon in fine-resolution images. Consequently, the predicted fine-resolution images lack intraclass variability and spatial details [25], [26]. On the other hand, the Bayesian-based method employs Bayesian estimation theory to probabilistically fuse images. Li et al. [27] utilized the Bayesian maximum entropy nonlinear geostatistical method to establish the error model for MODIS sea surface temperature and AMSR-E sea surface temperature at varying resolutions. Moreover, the dictionary-learning-based algorithm establishes a correspondence between fine-resolution and coarse-resolution images by utilizing structural similarity, enabling the capture of land cover type changes during prediction [28]. Despite the comprehensive consideration of changes in phenology and land cover by the Bayesian-based and dictionary-learning-based methods, they still fail to account for changes in heterogeneous landscapes [29]. In 2006, Gao et al. [30] introduced the spatiotemporal reflectance reconstruction via a multiscale fusion model (STARFM), employing window shifting and weighted

functions for pixel prediction. In 2010, Zhu et al. [31] presented enhanced STARFM (ESTARFM), which enhances the fusion performance of spatiotemporal fusion algorithms in heterogeneous areas through the introduction of transformation coefficients. Additionally, several other weighted function-based spatiotemporal fusion algorithms, including mESTARFM, SAD-FAT, ATPPK-STARFM, and ISKRFM, have been proposed. All of these algorithms predict phenological changes in homogeneous regions using the STARFM framework [32], [33], [34]. Nonetheless, weighted-function-based methods exhibit insufficient performance in predicting phenological changes and land cover changes in heterogeneous landscapes [35], [36].

In recent years, various mixed methods have been proposed for remote sensing applications. One such method is the flexible spatiotemporal data fusion (FSDAF), which represents a typical mixed approach. The FSDAF method combines spectral unmixing analysis, thin-plate spline (TPS) interpolation, and weighting functions to minimize input image requirements and improve the capability to predict heterogeneous changes [37], [38]. The TPS interpolator is utilized to predict daily land cover change information from high-temporal-resolution images. Therefore, FSDAF is capable of integrating challenging scenes, specifically the abrupt and drastic land cover changes occurring between input and predicted images: First, for highly mixed heterogeneous landscape elements, their reflectance changes can be estimated by solving linear mixing equations; second, for abrupt land cover changes, they can be captured through spatial interpolation if they appear in coarse images [39]. The FSDAF algorithm has gained wide application in recent years [40], [41].

Spatiotemporal fusion algorithms for remote sensing images have practical value in the field of remote sensing [42], [43], [44]. However, their application in marine remote sensing and intertidal zone monitoring is relatively limited [45]. In this study, we propose a novel method for monitoring intertidal zone terrain based on the FSDAF fusion algorithm. The method combines GOCI-II satellite data (500 m spatial resolution, 1-h temporal resolution) and Sentinel-2 satellite data (10 m spatial resolution, 5-day temporal resolution). An enhanced Normalized Difference Water Index (MNDWI) is used to differentiate between water and land within the intertidal zone. The accurate waterlines are obtained using Otsu threshold segmentation, and the intertidal zone pseudo-DEM is constructed. This method overcomes the limitations of traditional waterline methods, such as spatiotemporal contradiction in remote sensing images, which leads to a scarcity of waterlines, nonuniform distribution, and a wide image time span. Additionally, the proposed method improves the accuracy of intertidal zone terrain inversion by overcoming the limitation of constructing the intertidal zone DEM within a single day. The study aims to fuse short-time sequence images and invert intertidal zones to dynamically monitor muddy intertidal zone terrain elevation in coastal regions and investigate changes within the intertidal zone [46].

The structure of this study is illustrated in Fig. 2, which encompasses remote sensing image spatiotemporal fusion, waterline extraction, intertidal DEM inversion, and accuracy verification. The rest of this article is organized as follows. Section II introduces the intertidal study area located along the

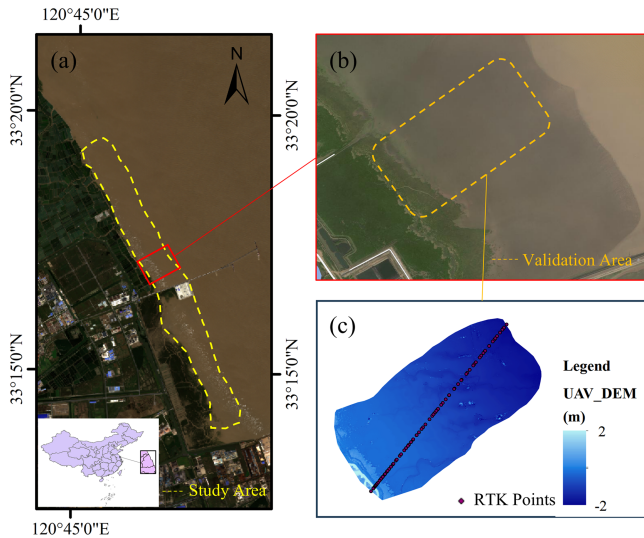


Fig. 1. (a) Yellow polygon represents the study area. (b) Red polygon denotes the zoomed-in region of (a), and the light yellow polygon indicates the validation area. (c) Area was measured based on a drone equipped with RTK technology, with the black dots representing the RTK samples collected by handheld devices.

coast of Yancheng City, Jiangsu Province, along with the field measurement dataset. Section III presents the proposed method for establishing the intertidal DEM inversion, including image preprocessing, spatiotemporal fusion, and tidal reconciliation model. Section IV provides the detailed results and validation of the inversion, including the analysis of annual intertidal evolution. Section V provides the discussion regarding the sources and limitations of errors and the impact of human activities on the morphological evolution of intertidal zones. Finally, Section VI concludes this article.

II. STUDY AREA AND DATASET

A. Study Area

The study area is located in Dafeng District, Yancheng City, the intertidal zone and the radiating sand ridge facing each other across the water [as shown in Fig. 1(a)]. The area lies between longitude $120^{\circ}41'5''$ and $120^{\circ}50'16''$ east and latitude $33^{\circ}13'40''$ and $33^{\circ}20'6''$ north, with a total area of 90.75 km^2 .

The Dafeng muddy intertidal zone features a gentle slope, with an average gradient of only 0.5% and a maximum width of 1–10 km. Due to the abundant supply of sediment from the Yellow River and Yangtze River estuaries, the sediment source in this region is rich. As a result, the intertidal zone exhibits significant and sustained geomorphic changes, characterized by pronounced fluctuations and evident erosion and deposition trends [47], [48], [49].

The selection of this area was based on the fact that the coastal zone of Jiangsu exhibits a transition regime from accretion to erosion, caused by the decreasing supply of sediment from the abandoned Yellow River over the years. The initial turning point between erosion and accretion was believed to be at Doulong Harbour. The northern part of the Doulong Harbour coast was already under full erosion conditions. Therefore, investigating

TABLE I
INFORMATION ON SENTINEL-2 AND GOCI-II IMAGES

Satellite	Date	Number of Scenes	Time (UTC-8)
Sentinel-2	10/10/2022	1	10:48
GOCI-II	29/09/2022	9	08:15
			09:15
			10:15
			11:15
			12:15
			13:15
			14:15
			15:15
			16:15

whether the tipping point is shifting southward is crucial to supporting Jiangsu's coastal economic planning and seawall reinforcement.

B. Satellite Image Dataset

In this study, Sentinel-2 and GOCI-II remote sensing optical images were selected as the data sources. The Sentinel-2 satellite is a high-resolution, multispectral imaging satellite with a spatial resolution of 10 m and a revisiting period shortened to five days. Sentinel-2 images were downloaded from the European Space Agency's Copernicus data hub (<https://scilb.copernicus.eu/dbus>). On the other hand, GOCI-II is a medium-resolution water color satellite with a spatial resolution of 500 m. The satellite generates an image every hour from 8:15 to 16:15 of UTC-8. GOCI-II images can be downloaded from the official website of the Korea Ocean Satellite Center (<https://www.nosc.go.kr/>).

Table I lists the image information used in this study; neighboring cloud-free images were selected through visual interpretation, including one Sentinel-2 image on October 10, 2022, and nine GOCI-II images on September 29, 2022.

C. RTK Dataset

This study utilized the CHC i50 engineering RTK system to collect the position information of sampling points, with a planar accuracy of $\pm(8 + 1 \times 10^{-6} \times D)$ mm and a height accuracy of $\pm(15 + 1 \times 10^{-6} \times D)$ mm. On September 29, 2022, RTK measurements were conducted to establish a straight line perpendicular to the coastline using a handheld device. Along this line, a total of 99 RTK sampling points were selected at 15-m intervals, resulting in the creation of a 1.5-km intertidal zone profile line [as shown in Fig. 1(c)].

D. Unmanned Aerial Vehicle (UAV) Dataset

The DJI Phantom 4 RTK version UAV was employed to obtain the image data of the validation area, with a horizontal accuracy of $1 \text{ cm} \pm 1 \text{ ppm}$ and a vertical accuracy of $1.5 \text{ cm} \pm 1 \text{ ppm}$. The DJI Phantom 4 RTK version utilizes RTK positioning technology to accurately measure intertidal wetland vegetation and obtain high-precision intertidal zone image data. The study

area was located on the north side of Dafeng Harbor Pier 1, with a flying area of approximately 1000 m². On September 25, 2022, more than 2000 images were acquired and processed using Pix4D software to generate DEM of the study area [as shown in Fig. 1(c)].

III. RESEARCH METHODOLOGY

A. Image Preprocessing

In order to address variations caused by sensor differences, atmospheric conditions, solar effects, and inherent noise, as well as to meet the specific analysis requirements of the study area, preprocessing of remote sensing images is essential [50]. This typically involves performing image correction and data resampling.

For Sentinel-2 data, the initial step involves radiometric calibration to convert the digital number values to radiance values, followed by atmospheric correction. GOCI-II data, on the other hand, requires the use of dedicated software called SNAP for processing. Since the raw data of GOCI-II are already calibrated through radiometric calibration, it undergoes further correction using the GLT geometric correction method.

The FSDAF algorithm necessitates that the input images have identical pixel size and image size [39]. Although the coarse-resolution image and the fine-resolution image may cover the same geographic location, an exact match in image size cannot be guaranteed. Moreover, since the FSDAF algorithm calculates weighted values based on the center pixel of the window, it is crucial to ensure that corresponding pixels between the coarse-resolution image and the fine-resolution image are aligned in the geographic location. Consequently, resampling the coarse-resolution image is necessary to achieve an equal pixel size to the fine-resolution image, resulting in images of the same size and geographic location.

B. Remote Sensing Image Spatiotemporal Fusion

In this study, the FSDAF algorithm was employed to merge remote sensing satellite images. The data sources consisted of GOCI satellite data, which had a spatial resolution of 500 m and a temporal resolution of 1 h, as well as Sentinel-2 data, which had a spatial resolution of 10 m and a temporal resolution of five days. The main objective was to generate short time-series products with a spatial resolution of 10 m and a temporal resolution of 1 h.

The fusion image algorithm utilized the FSDAF algorithm [as shown in Fig. 2(a)]. The process involved performing spectral supervised classification on a pair of remote sensing images. Subsequently, various coarse-resolution images were used to estimate the temporal changes in the classes. These changes were then used to predict the fine-resolution image and its residual using a TPS interpolator, which guided the distribution of the residual. Finally, the robust prediction result of the fine-resolution image was obtained by incorporating neighborhood information.

The fusion image was generated using the following equation:

$$F_2(x_{ij}, y_{ij}, b) = F_1(x_{ij}, y_{ij}, b) + \sum_{k=1}^m \omega_k \cdot \Delta F(x_k, y_k, b) \quad (1)$$

where $F_2(x_{ij}, y_{ij}, b)$ represents the predicted pixel value of the high-spatiotemporal-resolution satellite image at (x_{ij}, y_{ij}) , and $F_1(x_{ij}, y_{ij}, b)$ represents the pixel value of the high-spatial-resolution satellite image at (x_{ij}, y_{ij}) for the band b , the weight of distance ω_k , the predicted change of pixel value $\Delta F(x_k, y_k, b)$ in the band b at (x_{ij}, y_{ij}) , and m is the number of similar pixels.

C. T_Tide Model

The T_tide model, developed by Foreman using MATLAB, is a valuable tool for conducting harmonic analysis on tidal data for durations of one year or less, with a high level of accuracy [51].

In this study, the T-tide model was utilized to forecast tidal levels and determine waterline elevations based on the measured tidal data along the coastline. Tidal data were collected at 10-min intervals throughout the year 2022 (as shown in Fig. 3). The corresponding tidal levels at the time of the remote sensing image were identified, and a weighted average was computed to assign the values to the respective waterline.

D. Waterline Extraction

The process of waterline extraction from the imagery [as shown in Fig. 2(b)] consists of two main steps: First, distinguishing between water and land using the spectral index method; second, performing threshold segmentation to extract the water body.

In order to distinguish between water and nonwater pixels, a water index is required. In this study, an enhanced version of the normalized difference water index (MNDWI) was employed [52]. Laonamsai et al. [53] utilizing NDWI, MNDWI, SAVI, WRI, and AWEI for estimating erosion and deposition in Ping River in Thailand, MNDWI outperforms other indices in extracting water bodies. The formula for computing the MNDWI is presented as follows:

$$\text{MNDWI} = \frac{(\text{Green} - \text{MIR})}{(\text{Green} + \text{MIR})} \quad (2)$$

The green band is denoted as Green, while the middle infrared band is denoted as MIR. The MNDWI extraction results were binarized using the Otsu method [54]. This method determines a single intensity threshold to classify pixels into two categories: foreground and background. The threshold is determined by minimizing the within-class intensity variance or maximizing the between-class variance. However, it is important to note that the Otsu method is sensitive to noise and target size and is most effective for images exhibiting a unimodal between-class variance. The formula for computing the threshold is provided as follows:

$$\text{temp} = (h_0 - h_1)^2 \cdot w_1 + (h_0 - h_2)^2 \cdot w_2 \quad (3)$$

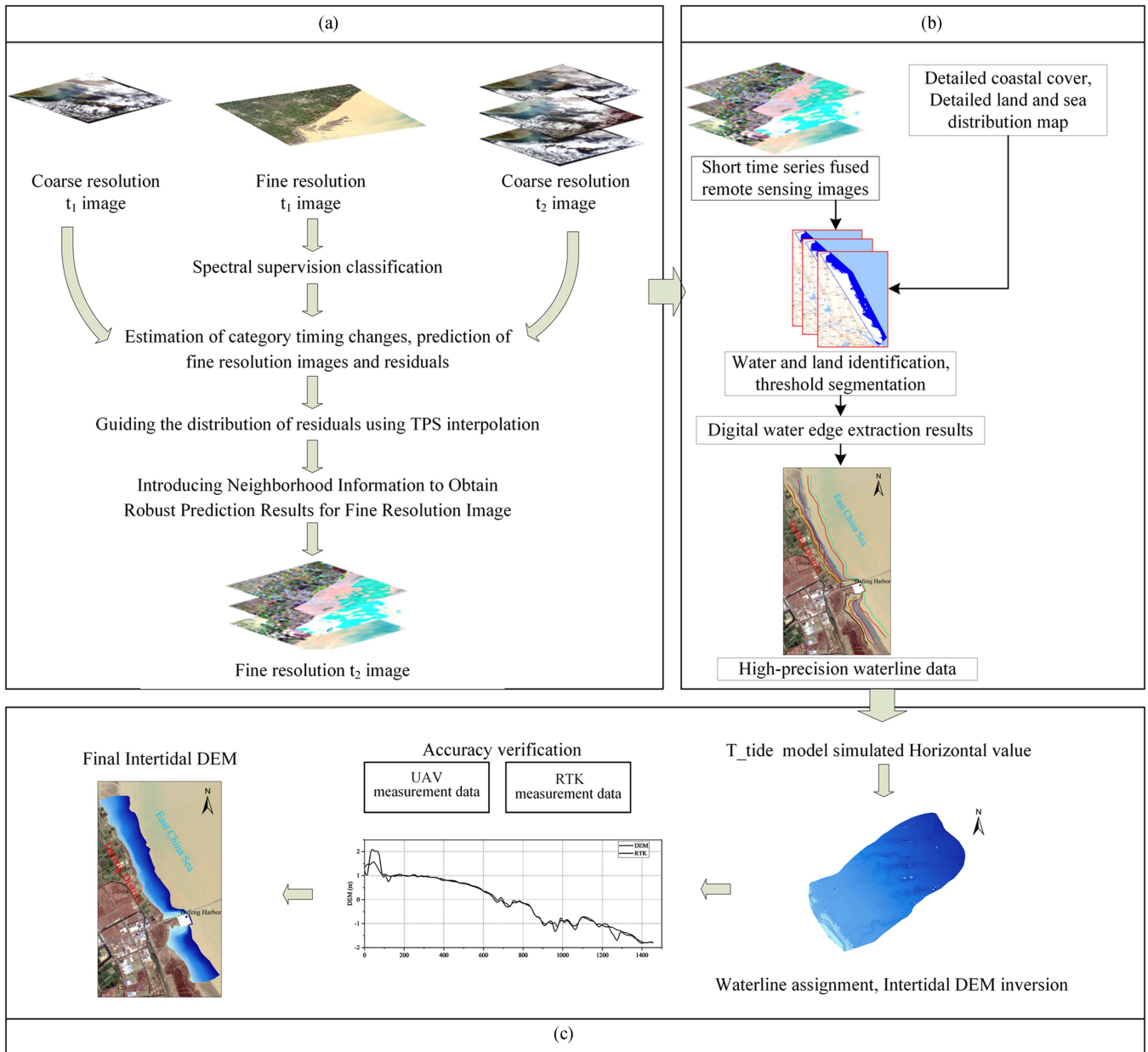


Fig. 2. Technical flowchart. (a) Spatiotemporal fusion of remote sensing image. (b) Waterline extraction. (c) Intertidal DEM inversion, DEM accuracy verification.

The threshold, represented as $temp$, is used to segment the image into foreground and background regions. h_0 denotes the overall average gray value of the image. The proportion of foreground pixels in the image is denoted as w_1 , with an average gray value of h_1 . Similarly, w_2 represents the proportion of background pixels in the image, with an average gray value of h_2 . To obtain the waterline after image threshold segmentation, the PAEK algorithm is employed for smoothing, ultimately resulting in the instantaneous waterline.

E. DEM Inversion in the Intertidal Zone

In 1995, Mason et al. [55] proposed the theory of waterline composite technique: assuming that the waterline is an isohypse,

a pseudo-DEM of tidal flats is generated by overlaying waterlines under different tidal conditions. DEM usually uses two models: regular grid model and irregular triangular network. In grid DEM in flat terrain, there is a large amount of data redundancy, and it is difficult to express the complexity of the terrain of the phenomenon of mutation; TIN can be changed with the complexity of the terrain undulation changes in the density of the sampling points and decide the location of the sampling points to supplement the defects of the grid model; the DEM is in ArcGIS 10.7 using the 3-D extension module to use irregular triangles generated by interpolation. It selects Delaunay triangulation to connect irregularly spaced elevation point data for interpolation, and then interpolates the elevation triangles into the grid-based DTM [as shown in Fig. 2(c)]. The

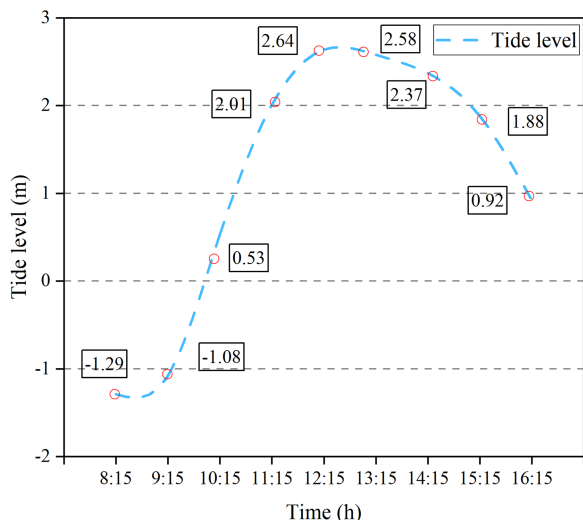


Fig. 3. Simulated tide values corresponding to the time using the T-tide model.

study aimed to enhance the accuracy of the inversion process by increasing the number of waterlines, achieving a more uniform spatial coverage and reducing the time interval between captured images.

IV. RESULTS

A. Results of Spatiotemporal Fusion

The findings of the algorithmic fusion are illustrated in Fig. 4, which displays a series of nine images taken at hourly intervals from 8:15 to 16:15 on September 29, 2022. The tide was at its lowest point at 8:15, resulting in the complete exposure of the intertidal zone. Subsequently, the tide gradually moved toward the land, reaching its highest point at 12:15, when the intertidal zone was fully submerged by seawater. The FSDAF algorithm effectively preserves both the color and contour information of the built-up areas in the images, while accurately capturing the dynamic changes in the features of interest, such as variations in water surfaces caused by different reflectance properties of the water bodies. These distinctions are clearly visible in the fused images.

In particular, the fused images of the intertidal zone and GOCI-II intertidal zone demonstrate a strong agreement during the period of intertidal exposure (as shown in Fig. 5). This observation confirms the fusion algorithm's capability to precisely capture the evolution of the intertidal zone with improved spatial resolution.

B. Results of Waterline Extraction

Fig. 6 presents the outcomes of waterline extraction from the fusion images. The waterline attained its minimum level at 8:15 and reached its maximum at 12:15. However, during the period between 12:15 and 14:15, when the tide was at its peak and the entire intertidal zone was submerged, seawater accumulated along the embankment, resulting in waterline extraction outcomes that were nearly indistinguishable. To compare and

analyze these findings, the waterline positions at high and low tide were aligned with the tidal curve of the DaFeng Harbor area on September 29, 2022 (as shown in Fig. 6). Remarkably, based on Fig. 3, we can find that the waterline positions at both high and low tide precisely corresponded to the measured tidal values.

C. DEM Validation

Fig. 7 presents the DEM of the intertidal zone, which was obtained through inversion techniques. Also, utilize the DEM area adjacent to the shore as the upper portion of the intertidal zone and the DEM area near the sea as its lower portion. The DEM covers an elevation range from -1.29 to 2.64 m and is represented using a color scale that transitions from light to dark, indicating the transition from land to ocean. However, it is important to note that the extraction of waterlines and simulation of water level values during the generation of the DEM can introduce errors. Therefore, conducting a precision evaluation is crucial to assess the quality of the DEM generation and ensure consistency with the actual conditions.

The precision analysis involves two methods: RTK profile line precision verification and UAV DEM validation. In the RTK profile line precision verification, RTK data obtained from measurements are imported into ArcGIS software. These data are used to generate 99 RTK measurement points. The elevation values of the waterline inversion DEM are extracted at the corresponding positions of these RTK measurement points. A point comparison diagram (as shown in Fig. 8) is then created, where a correlation coefficient closer to 1 indicates better results. The trend of the inversion DEM elevation values aligns well with that of the RTK profile line elevation values, exhibiting a correlation coefficient of 0.96. This indicates a relatively ideal performance of the waterline inversion DEM. However, it should be noted that the largest error occurs near the Seawall, which is due to the fact that the water level at a distance of 50 m from the Seawall has exceeded the maximum tidal level at 12:15, 13:15, and 14:15, resulting in higher elevation values near the Seawall. Consequently, a greater error is generated. The overall error range of the profile line comparison is ± 0.3 m.

The validation of the unmanned aerial vehicle digital elevation model (UAV-DEM) was conducted using the ArcGIS raster calculator. The discrepancy between the UAV measurement area (as shown in Fig. 9) and the generated waterline DEM was computed to accurately determine the error between the generated DEM and the actual waterline measurement. The elevation of the UAV measurement area is closely aligned with that of the waterline inversion DEM after classification. The root-mean-square error in the final difference map was found to be 0.28 m (as shown in Fig. 10), with a maximum error range of -0.25 m to 0.25 m, accounting for 84% of the total discrepancies. Among these, errors ranging from -0.25 m to 0 m constituted 39%, while errors ranging from 0 to 0.25 m constituted 45% (as shown in Fig. 11). Therefore, it can be concluded that the data generated by the waterline inversion method are reliable. The primary errors were concentrated at the Seawall and the lowest waterline. The Seawall error was

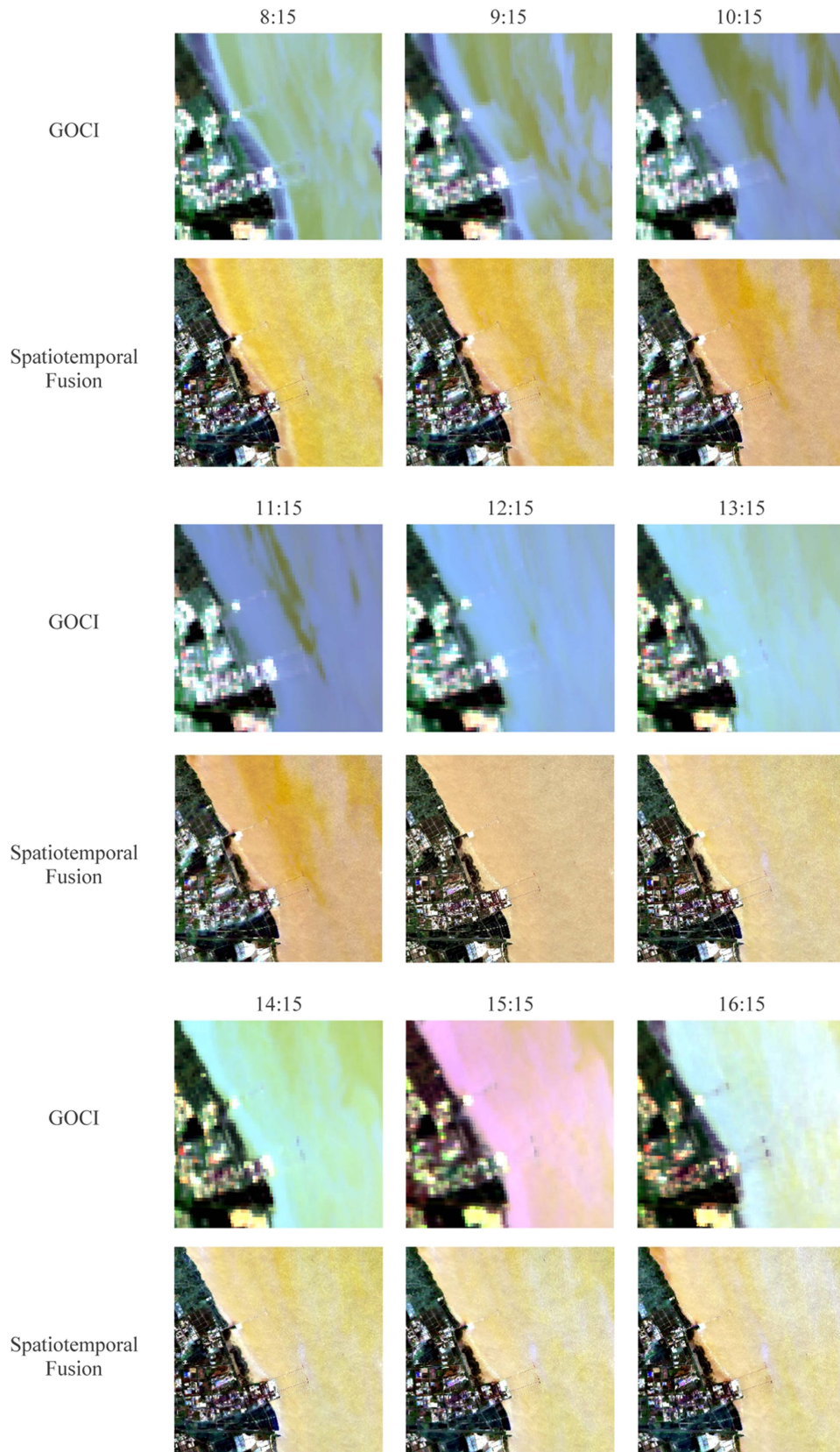


Fig. 4. Fusion of remote sensing images from different time periods within the research area.



Fig. 5. Moments of high tide when intertidal zones are exposed. (a) Represents the moment of high tide captured by GOCI-II. (b) Represents the moment of high tide captured by the fusion image. The red polygon indicates the intertidal zone.

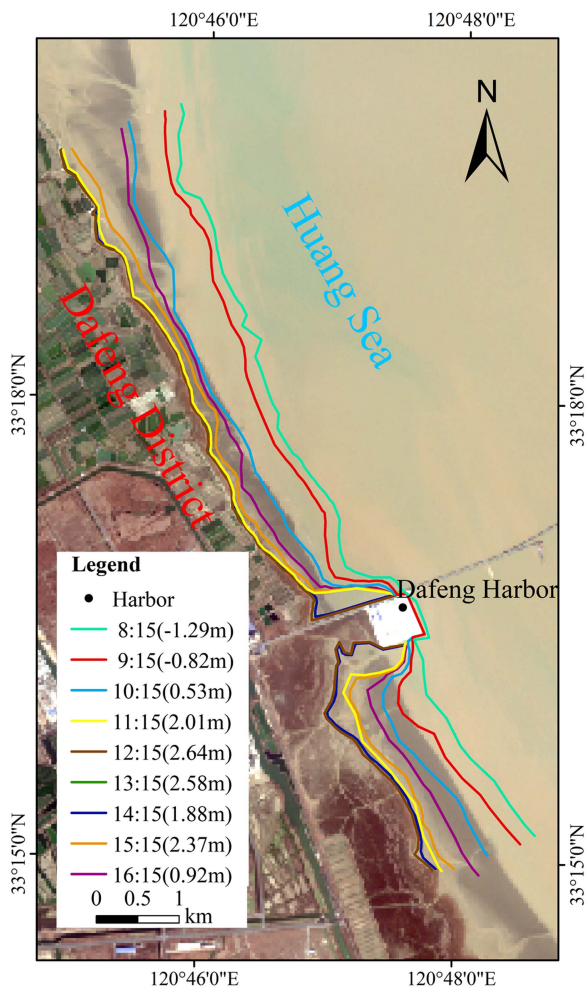


Fig. 6. Waterline extracted from the fused images.

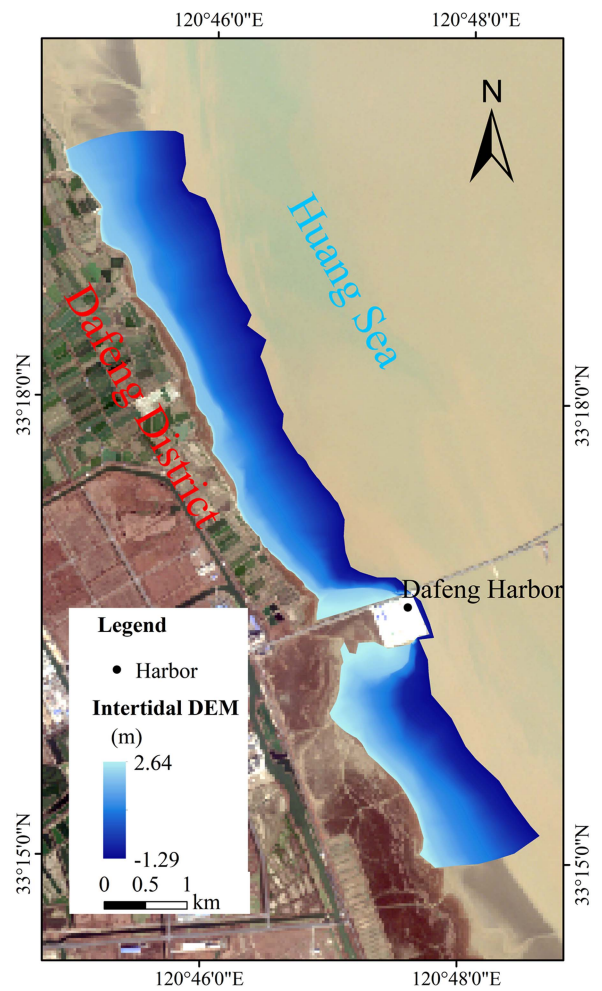


Fig. 7. DEM generated by the waterline inversion.

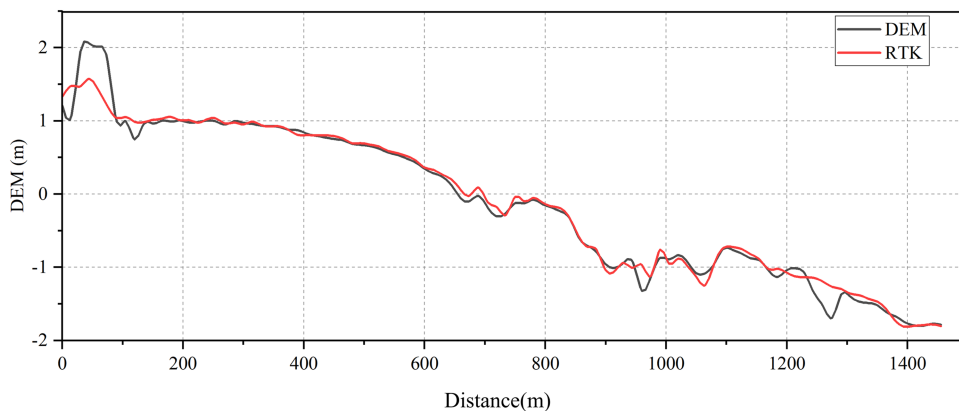


Fig. 8. Cross-sectional comparison graph. The comparison between the RTK sampling points [as shown in Fig. 1(c)] and the inverted intertidal zone at the same location.

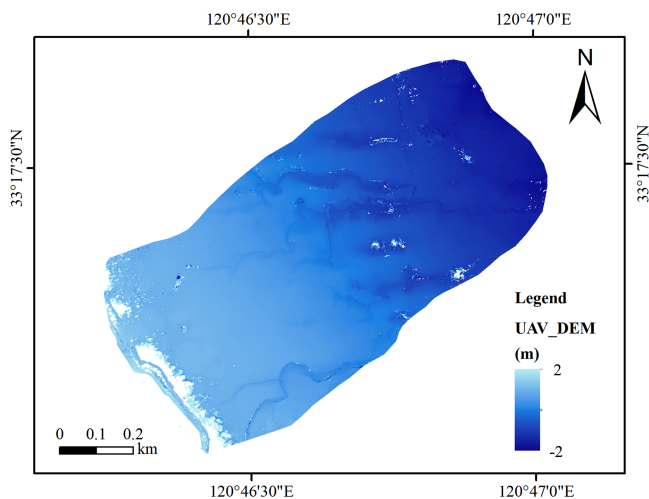


Fig. 9. Intertidal zone of the north side of Dafeng harbor pier 1 in Dafeng district, Yancheng, generated by UAVs.

attributed to the dense growth of *Spartina alterniflora* during the UAV aerial survey, where the elevation of *Spartina alterniflora* was mistakenly identified as the intertidal elevation, resulting in significant deviation near the Seawall. Additionally, the error at the lowest waterline was caused by the interpolation of elevation values in this area, introducing inaccuracies. Furthermore, errors were also present in the middle of the difference. The red area indicated an error caused by the presence of a tidal channel, while the blue point-like area represented a newly identified mesoscale landform unit known as a hummocky patch, generated by erosion and typically exhibiting a height of 30–40 cm [56].

D. Annual Variation of Intertidal Zone

In order to investigate the annual evolution of the intertidal zone in the study area, the data from 2023 years of Sentinel-2 and GOCI-II images were utilized. By employing the FSDAF algorithm, we were able to fusion remote sensing images from nine different time periods on March 26, 2023, ranging from

8:15 to 16:15. This fusion process allowed us to generate a comprehensive intertidal zone map for that specific day.

To determine the annual variation of the intertidal zone, we subtracted the DEM of 2022 from the DEM of 2023 (as shown in Fig. 12). Positive sedimentation rates were classified as accretion, while negative sedimentation rates were classified as erosion. The overall trend in the intertidal zone from 2022 to 2023 indicated a pattern of accretion, with the exception of the southern part of the harbor. In this specific area, the upper region exhibited accretion, while the middle and lower regions experienced erosion. The most significant erosion was observed in the middle part of the intertidal zone, with a maximum erosion depth of 1 m at the bottom. This erosion can be attributed to the diversion of the Yellow River, which previously transported a substantial amount of sediment into Jiangsu, resulting in continuous accretion and seaward expansion of the intertidal zone [57]. However, as the Yellow River now flows into Shandong, the supply of sediment has diminished, leading to gradual erosion of the intertidal zone in Jiangsu from south to north. The observed accretion in the upper intertidal zone and erosion in the lower intertidal zone, which is consistent with Chen et al.'s [58] study, show that the slope of coastal mudflats in Jiangsu is increasing. In the southern part of the harbor, accretion trends were influenced by the sediment accumulation facilitated by the piers 1 and piers 2 in Dafeng Harbor. This resulted in sediment accumulation between the piers and increased accretion toward the land, particularly the neighborhood of the pier [59].

V. DISCUSSION

A. Sources and Limitations of Errors

The results obtained from the T_tide model are prone to errors due to its inherent inaccuracies in predicting tidal values. This model can only provide harmonic constants, which represent amplitude and phase that remain constant over time. However, in reality, tidal and nontidal processes, such as river runoff, exhibit nonlinear interactions that can cause rapid changes in amplitude and phase within short-time periods. As a result, the T_tide model is not suitable for analyzing situations where such nonlinear interactions occur, and it is only applicable for

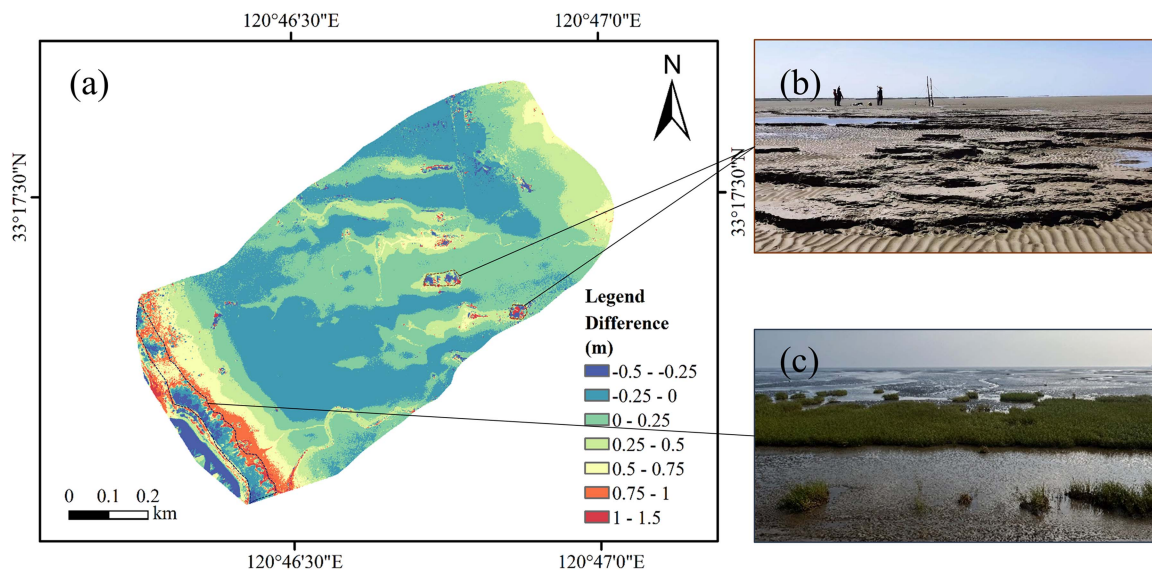


Fig. 10. (a) Denoting the difference between the UAV-DEM and the intertidal zone DEM generated from the waterline inversion. (b) Indicating the hummocky patches. (c) Referring to the intertidal meadow (*spartina alterniflora*) community near the seawall in the study area.

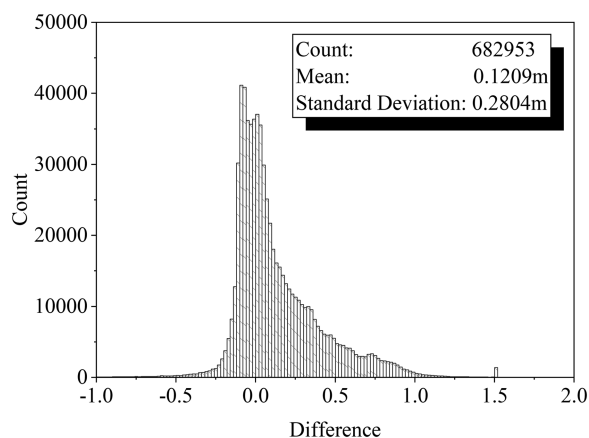


Fig. 11. Statistical analysis of the difference.

stationary tides. Consequently, when dealing with nonstationary tides, errors can be introduced, leading to deviations in the final topographic inversion results.

The FSDAF algorithm, which is a robust weighted sum model used for image fusion, significantly modifies the image fusion process in the spectral domain. However, Zhao et al.'s [60] research indicates that the algorithm faces challenges when predicting changes in heterogeneous terrain and land cover, despite accurately predicting physical changes in homogeneous areas. Additionally, the accuracy of the terrain is affected by geographical positioning errors, making it difficult for the algorithm to fully capture the true intertidal topography.

Another limitation of this algorithm is the loss of fine-scale details during the fusion process. This occurs because the two fused images, GOCI and Sentinel, have substantially different spatial resolutions of 500 m and 10 m, respectively. The GOCI image elements are unable to depict small-scale changes in the

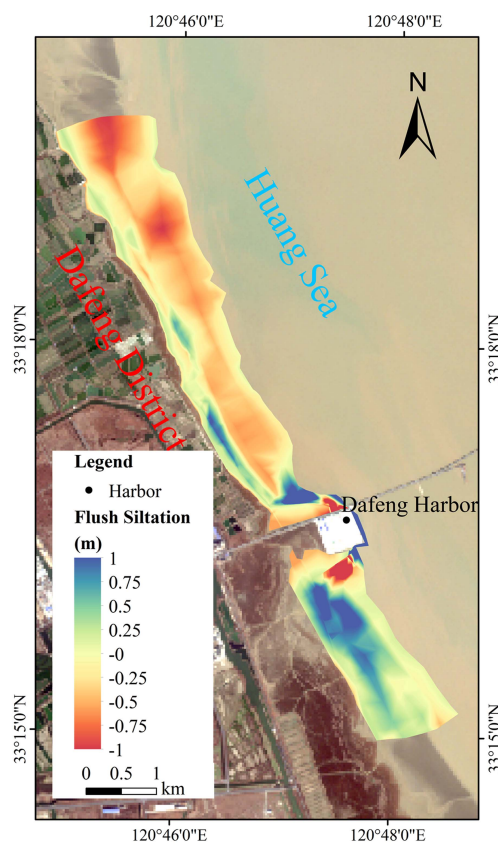


Fig. 12. Scour and Silt map. In this area, the upper region exhibited accretion, while the middle and lower regions experienced erosion. The most significant erosion was observed in the middle part of the intertidal zone, with a maximum erosion depth of 1 m at the bottom.

fused image, resulting in the omission of subtle variations in the intertidal zone. Furthermore, the spatial resolution of the remote sensing image serves as a limiting factor in the quality of

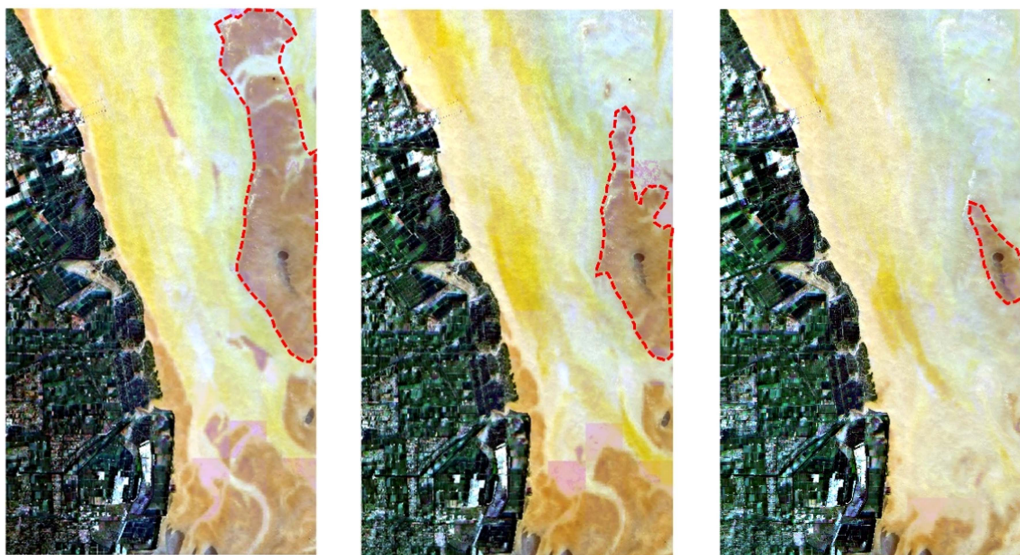


Fig. 13. Radiating sand ridge FSDAF fusion map with a red circle indicating the radiation sand ridge, which is gradually submerged over time.

intertidal inversion. According to Gao et al. [45], higher spatial resolutions of satellite images correspond to improved accuracy and reliability in constructing DTMs.

Moreover, for this study, high-tide-level remote sensing images are necessary for image fusion. The use of low-tide-level high-resolution imagery would result in fused images of bare low-tide-level intertidal zones overlaying the high-tide-level low-resolution imagery. This would result in intertidal zones that were originally submerged by seawater at the high-tide-level appearing as intertidal zones in the results of the fused images; an overlap that made it impossible to extract the waterline and, although the fusion of the images was successful, the changes in each image were not significant. However, the fusion algorithm may be more suitable for areas with obvious changes, such as the nearby radiated sandbar in the study area. By selecting time periods with significant changes, the changes in the intertidal zone are prominent and consistent with the trend in the tide table (as shown in Fig. 13).

B. Impact of Human Activities on the Morphological Evolution of Intertidal Zones

Dafeng District in Yancheng City is a significant component of the Yangtze River Delta Economic Zone in central Jiangsu Province. The morphological evolution of the intertidal zone in this region is influenced by various factors, including human activities, such as reduced sediment supply from rivers, reclamation, the redrawn blueprint of the Yangtze River Delta, and the northward diversion of the Yellow River [61], [62].

First, the reduced sediment supply from rivers is one of the major factors affecting the morphological evolution of the intertidal zone in Dafeng District, Yancheng City [63]. Rivers are the surface water systems, and sediment at river mouths is a crucial factor for maintaining the stability of the intertidal ecosystem. However, human activities have significantly reduced the sediment supply from rivers, resulting in the morphological

evolution of the intertidal zone [64], [65]. For instance, local agricultural production and urban development have caused massive land cultivation and coverage, which destroyed the original vegetation and land structure, intensified soil erosion, and reduced the sediment supply capacity of rivers [66].

Second, reclamation is another factor affecting the morphological evolution of the intertidal zone in Dafeng District, Yancheng City [67], [68]. Over the past few decades, large-scale reclamation has altered the coastline and thereby affected the balance of the intertidal ecosystem. These reclamation activities have reduced the supply of sediment while also accelerating the flow velocity of the tidal current, leading to the severe scouring and erosion of the intertidal zone [69].

Finally, the redrawn blueprint of the Yangtze River Delta has also affected the morphological evolution of the intertidal zone in Dafeng District, Yancheng City. The plan aims to promote large-scale economic development and urbanization in the Yangtze River Delta region, involving massive infrastructure construction and land transformation, which has impacted the intertidal zone's morphology [70].

VI. CONCLUSION

The monitoring of rapid changes in intertidal wetland topography is of great importance in the context of global climate change and information exchange. Intertidal wetlands provide valuable ecosystem services that benefit both human and nonhuman inhabitants, highlighting the need to understand the spatial evolution of intertidal terrain. Therefore, the objective of this study is to utilize the FSDAF algorithm to combine high-resolution Sentinel-2 imagery with high-temporal-resolution GOCI-II remote sensing image products. This approach allows for the generation of fusion images with a spatial resolution of 10 m and hourly time series depicting different tidal levels. The MNDWI water index and Otsu method were specifically employed to accurately identify and extract water boundaries during the

construction of the intertidal DEM, enabling the analysis of dynamic changes in intertidal land over time.

To verify and analyze the accuracy of the results, this study utilized RTK profiles and drone survey data of intertidal wetlands in the study area. The findings demonstrate a strong correlation (0.9595) and close alignment between the water edge inversion DEM and the RTK profile line. Furthermore, when compared with the drone data, the root-mean-square error is 0.2803 m, with the majority of errors (84%) falling within the range of -0.25 m to 0.25 m. These results support the future application of fusion monitoring methods for studying the evolution of intertidal terrain in the entire Jiangsu intertidal zone. The study confirms that the FSDAF spatiotemporal fusion method not only ensures the quality of intertidal DEM inversion but also addresses the limitations posed by limited high-spatial-resolution satellite image time series due to cloud cover and low revisit frequency. It effectively mitigates the impact of time series and spatial resolution on DEM quality, demonstrating the efficacy of the spatiotemporal fusion algorithm in monitoring the dynamic changes in intertidal wetland topography. Furthermore, this study investigated the annual terrain evolution of intertidal zones and observed an overall trend of accretion in the Dafeng District. The study discusses contributing factors, such as reduced sediment supply, land reclamation, the revision of the Yangtze River Delta blueprint, and the northward movement of the Yellow River. The fusion monitoring method not only facilitates the development of coastal planning projects related to intertidal zones but also provides insights into the response processes and mechanisms of intertidal systems to natural and human-induced disturbances.

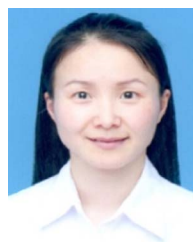
ACKNOWLEDGMENT

The authors would like to thank the United States ITT VIS, Company, for providing ENVI5.5.

REFERENCES

- [1] M. L. Kirwan and J. P. Megonigal, "Tidal wetland stability in the face of human impacts and sea-level rise," *Nature*, vol. 504, no. 7478, pp. 53–60, Dec. 2013.
- [2] M. Mahdianpari et al., "A large-scale change monitoring of wetlands using time series Landsat imagery on Google Earth engine: A case study in Newfoundland," *GIScience Remote Sens.*, vol. 57, no. 8, pp. 1102–1124, 2020.
- [3] E. Brand, M. Chen, and A.-L. Montreuil, "Optimizing measurements of sediment transport in the intertidal zone," *Earth-Sci. Rev.*, vol. 200, 2020, Art. no. 103029.
- [4] L. H. L. Loke, R. A. Chisholm, and P. A. Todd, "Effects of habitat area and spatial configuration on biodiversity in an experimental intertidal community," *Ecology*, vol. 100, no. 8, Aug. 2019, Art. no. e02757.
- [5] J. Catalao and G. Nico, "Multitemporal backscattering logistic analysis for intertidal bathymetry," *IEEE Trans. Geosci. Remote Sens.*, vol. 55, no. 2, pp. 1066–1073, Feb. 2017.
- [6] E. Alevizos and D. D. Alexakis, "Monitoring short-term morphobathymetric change of nearshore seafloor using drone-based multispectral imagery," *Remote Sens.*, vol. 14, no. 23, 2022, Art. no. 6035.
- [7] S. Maiti and A. K. Bhattacharya, "Shoreline change analysis and its application to prediction: A remote sensing and statistics based approach," *Mar. Geol.*, vol. 257, no. 1/4, pp. 11–23, 2009.
- [8] J. T. Kelly and A. M. Gontz, "Using GPS-surveyed intertidal zones to determine the validity of shorelines automatically mapped by Landsat water indices," *Int. J. Appl. Earth Observ. Geoinf.*, vol. 65, pp. 92–104, 2018.
- [9] H. Huang, Y.-P. Wang, S. Gao, J. Chen, Y. Yang, and J.-H. Gao, "Extraction of morphometric bedform characteristics from profiling sonar datasets recorded in shallow coastal waters of China," *China Ocean Eng.*, vol. 26, no. 3, pp. 469–482, 2012.
- [10] Y. Gao et al., "Hyperspectral and multispectral classification for coastal wetland using depthwise feature interaction network," *IEEE Trans. Geosci. Remote Sens.*, vol. 60, 2021, Art. no. 5512615.
- [11] S.-E. Park, W. M. Moon, and D.-J. Kim, "Estimation of surface roughness parameter in intertidal mudflat using airborne polarimetric SAR data," *IEEE Trans. Geosci. Remote Sens.*, vol. 47, no. 4, pp. 1022–1031, Apr. 2009.
- [12] G. Heygster, J. Dannenberg, and J. Notholt, "Topographic mapping of the German tidal flats analyzing SAR images with the waterline method," *IEEE Trans. Geosci. Remote Sens.*, vol. 48, no. 3, pp. 1019–1030, Mar. 2010.
- [13] S. Vitousek et al., "The future of coastal monitoring through satellite remote sensing," *Cambridge Prisms, Coastal Futures*, vol. 1, 2023, Art. no. e10.
- [14] M. K. Ghosh, L. Kumar, and C. Roy, "Monitoring the coastline change of Hatiya Island in Bangladesh using remote sensing techniques," *ISPRS J. Photogramm. Remote Sens.*, vol. 101, pp. 137–144, 2015.
- [15] K. Vos, K. D. Splinter, M. D. Harley, J. A. Simmons, and I. L. Turner, "CoastSat: A Google Earth engine-enabled python toolkit to extract shorelines from publicly available satellite imagery," *Environ. Model. Softw.*, vol. 122, 2019, Art. no. 104528.
- [16] J.-H. Ryu, C.-H. Kim, Y.-K. Lee, J.-S. Won, S.-S. Chun, and S. Lee, "Detecting the intertidal morphologic change using satellite data," *Estuarine, Coastal Shelf Sci.*, vol. 78, no. 4, pp. 623–632, 2008.
- [17] X. Wang et al., "Tracking annual changes of coastal tidal flats in China during 1986–2016 through analyses of Landsat images with Google Earth engine," *Remote Sens. Environ.*, vol. 238, Mar. 2020, Art. no. 110987.
- [18] P. Letortu et al., "Retreat rates, modalities and agents responsible for erosion along the coastal chalk cliffs of Upper Normandy: The contribution of terrestrial laser scanning," *Geomorphology*, vol. 245, pp. 3–14, 2015.
- [19] J. M. Fitton, A. F. Rennie, J. D. Hansom, and F. M. E. Muir, "Remotely sensed mapping of the intertidal zone: A sentinel-2 and Google Earth engine methodology," *Remote Sens. Appl., Soc. Environ.*, vol. 22, 2021, Art. no. 100499.
- [20] Y. Liu, M. Li, M. Zhou, K. Yang, and L. Mao, "Quantitative analysis of the waterline method for topographical mapping of tidal flats: A case study in the Dongsha sandbank, China," *Remote Sens.*, vol. 5, no. 11, pp. 6138–6158, 2013.
- [21] E. Salameh et al., "Monitoring beach topography and nearshore bathymetry using spaceborne remote sensing: A review," *Remote Sens.*, vol. 11, no. 19, 2019, Art. no. 2212.
- [22] E. Salameh et al., "Monitoring sea level and topography of coastal lagoons using satellite radar altimetry: The example of the Arcachon Bay in the Bay of Biscay," *Remote Sens.*, vol. 10, no. 2, 2018, Art. no. 297.
- [23] X. Zhu, F. Cai, J. Tian, and T. K.-A. Williams, "Spatiotemporal fusion of multisource remote sensing data: Literature survey, taxonomy, principles, applications, and future directions," *Remote Sens.*, vol. 10, no. 4, 2018, Art. no. 527.
- [24] J. Wei, L. Wang, P. Liu, and W. Song, "Spatiotemporal fusion of remote sensing images with structural sparsity and semi-coupled dictionary learning," *Remote Sens.*, vol. 9, no. 1, 2016, Art. no. 21.
- [25] J. Wang and B. Huang, "A rigorously-weighted spatiotemporal fusion model with uncertainty analysis," *Remote Sens.*, vol. 9, no. 10, 2017, Art. no. 990.
- [26] M. Wu, W. Huang, Z. Niu, and C. Wang, "Generating daily synthetic Landsat imagery by combining Landsat and MODIS data," *Sensors*, vol. 15, no. 9, pp. 24002–24025, Sep. 2015.
- [27] B. Li, L. Han, and L. Li, "A spatiotemporal fusion network to multi source heterogeneous data for landslide recognition," *ISPRS Ann. Photogramm. Remote Sens. Spatial Inf. Sci.*, vol. 10, pp. 77–84, 2022.
- [28] H. Song, Q. Liu, G. Wang, R. Hang, and B. Huang, "Spatiotemporal satellite image fusion using deep convolutional neural networks," *IEEE J. Sel. Topics Appl. Earth Observ. Remote Sens.*, vol. 11, no. 3, pp. 821–829, Mar. 2018.
- [29] Z. Wang, Y. Ma, and Y. Zhang, "Review of pixel-level remote sensing image fusion based on deep learning," *Inf. Fusion*, vol. 90, pp. 36–58, 2023.
- [30] F. Gao, J. Masek, M. Schwaller, and F. Hall, "On the blending of the Landsat and MODIS surface reflectance: Predicting daily Landsat surface reflectance," *IEEE Trans. Geosci. Remote Sens.*, vol. 44, no. 8, pp. 2207–2218, Aug. 2006.

- [31] X. Zhu, J. Chen, F. Gao, X. Chen, and J. G. Masek, "An enhanced spatial and temporal adaptive reflectance fusion model for complex heterogeneous regions," *Remote Sens. Environ.*, vol. 114, no. 11, pp. 2610–2623, 2010.
- [32] D. Fu, B. Chen, J. Wang, X. Zhu, and T. Hilker, "An improved image fusion approach based on enhanced spatial and temporal the adaptive reflectance fusion model," *Remote Sens.*, vol. 5, no. 12, pp. 6346–6360, 2013.
- [33] Q. Weng, P. Fu, and F. Gao, "Generating daily land surface temperature at Landsat resolution by fusing Landsat and MODIS data," *Remote Sens. Environ.*, vol. 145, pp. 55–67, 2014.
- [34] B. Wu, B. Huang, K. Cao, and G. Zhuo, "Improving spatiotemporal reflectance fusion using image inpainting and steering kernel regression techniques," *Int. J. Remote Sens.*, vol. 38, no. 3, pp. 706–727, 2016.
- [35] Y. Pan, F. Shen, and X. Wei, "Fusion of Landsat-8/OLI and GOCI data for hourly mapping of suspended particulate matter at high spatial resolution: A case study in the Yangtze (Changjiang) estuary," *Remote Sens.*, vol. 10, no. 2, 2018, Art. no. 158.
- [36] F. Maselli, M. Chiesi, and M. Pieri, "A new method to enhance the spatial features of multitemporal NDVI image series," *IEEE Trans. Geosci. Remote Sens.*, vol. 57, no. 7, pp. 4967–4979, Jul. 2019.
- [37] J. Li, M. Ke, Y. Ma, and J. Cui, "Remote monitoring of NH₃-N content in small-sized inland waterbody based on low and medium resolution multi-source remote sensing image fusion," *Water*, vol. 14, no. 20, 2022, Art. no. 3287.
- [38] H. Gao et al., "cuFSDAF: An enhanced flexible spatiotemporal data fusion algorithm parallelized using graphics processing units," *IEEE Trans. Geosci. Remote Sens.*, vol. 60, 2021, Art. no. 4403016.
- [39] X. Zhu, E. H. Helmer, F. Gao, D. Liu, J. Chen, and M. A. Lefsky, "A flexible spatiotemporal method for fusing satellite images with different resolutions," *Remote Sens. Environ.*, vol. 172, pp. 165–177, 2016.
- [40] M. Liu et al., "An improved flexible spatiotemporal data fusion (IFS-DAF) method for producing high spatiotemporal resolution normalized difference vegetation index time series," *Remote Sens. Environ.*, vol. 227, pp. 74–89, 2019.
- [41] S. Liu, J. Zhou, Y. Qiu, J. Chen, X. Zhu, and H. Chen, "The FIRST model: Spatiotemporal fusion incorporating spectral autocorrelation," *Remote Sens. Environ.*, vol. 279, 2022, Art. no. 113111.
- [42] Y. Zhao and D. Liu, "A robust and adaptive spatial-spectral fusion model for PlanetScope and Sentinel-2 imagery," *GIScience Remote Sens.*, vol. 59, no. 1, pp. 520–546, 2022.
- [43] I. Fairley, A. Mendzil, M. Togneri, and D. Reeve, "The use of unmanned aerial systems to map intertidal sediment," *Remote Sens.*, vol. 10, no. 12, 2018, Art. no. 1918.
- [44] M. L. Zoffoli et al., "Sentinel-2 remote sensing of *Zostera* Noltedominated intertidal seagrass meadows," *Remote Sens. Environ.*, vol. 251, 2020, Art. no. 112020.
- [45] W. Gao et al., "Monitoring terrain elevation of intertidal wetlands by utilising the spatial-temporal fusion of multi-source satellite data: A case study in the Yangtze (Changjiang) Estuary," *Geomorphology*, vol. 383, 2021, Art. no. 107683.
- [46] Z. Yin et al., "Spatiotemporal fusion of land surface temperature based on a convolutional neural network," *IEEE Trans. Geosci. Remote Sens.*, vol. 59, no. 2, pp. 1808–1822, Feb. 2021.
- [47] J. Jia, Y. Wang, S. Gao, A. Wang, and Z. Li, "Interpreting grain-size trends associated with bedload transport on the intertidal flats at Dafeng, central Jiangsu coast," *Chin. Sci. Bull.*, vol. 51, no. 3, pp. 341–351, 2006.
- [48] F. Xing, Y. P. Wang, and J. Jia, "Hydrodynamics and sediment transport patterns on intertidal flats along middle Jiangsu coast," *Anthropocene Coasts*, vol. 5, no. 1, 2022, Art. no. 12.
- [49] S. Sharma, A. Paul, D. Mitra, and P. Chauhan, "Semi-automated workflow for mapping the extent and elevation profile of intertidal zone of parts of gulf of Kutch, India, using Landsat time series data," *J. Indian Soc. Remote Sens.*, vol. 49, no. 6, pp. 1343–1363, 2021.
- [50] Y. Li, H. Wu, H. Chen, and X. Zhu, "A robust framework for resolution enhancement of land surface temperature by combining spatial downscaling and spatiotemporal fusion methods," *IEEE Trans. Geosci. Remote Sens.*, vol. 61, Jun. 2023, Art. no. 4404514.
- [51] R. Pawlowicz, B. Beardsley, and S. Lentz, "Classical tidal harmonic analysis including error estimates in MATLAB using T_TIDE," *Comput. Geosci.*, vol. 28, no. 8, pp. 929–937, 2002.
- [52] C. Jürgens, "The modified normalized difference vegetation index (mNDVI) a new index to determine frost damages in agriculture based on Landsat TM data," *Int. J. Remote Sens.*, vol. 18, pp. 3583–3594, 1997.
- [53] J. Laonamsai et al., "Utilizing NDWI, MNDWI, SAVI, WRI, and AWEI for estimating erosion and deposition in Ping River in Thailand," *Hydrology*, vol. 10, no. 3, 2023, Art. no. 70.
- [54] N. Otsu, "A threshold selection method from gray-level histograms," *IEEE Trans. Syst., Man, Cybern.*, vol. 9, no. 1, pp. 62–66, Jan. 1979.
- [55] D. Mason, I. Davenport, G. Robinson, R. Flather, and B. McCartney, "Construction of an inter-tidal digital elevation model by the 'water-line' method," *Geophysical Res. Lett.*, vol. 22, pp. 3187–3190, 1995.
- [56] S. Zhu et al., "The hummocky patches and associated sediment dynamics over an accretional intertidal flat," *Front. Earth Sci.*, vol. 10, 2022, Art. no. 908351.
- [57] M. Su, P. Yao, Z. B. Wang, C. K. Zhang, and M. J. Stive, "Exploratory morphodynamic modeling of the evolution of the Jiangsu coast, China, since 1855: Contributions of old Yellow River-derived sediment," *Mar. Geol.*, vol. 390, pp. 306–320, 2017.
- [58] G. Chen et al., "Spatiotemporal mapping of salt marshes in the intertidal zone of China during 1985–2019," *J. Remote Sens.*, vol. 2022, 2022, Art. no. 9793626.
- [59] D. Chen, Y. Wang, H. Huang, C. Chen, and C. Yuan, "A behavior-oriented formula to predict coastal bathymetry evolution caused by coastal engineering," *Continental Shelf Res.*, vol. 135, pp. 47–57, 2017.
- [60] Y. Zhao, B. Huang, and H. Song, "A robust adaptive spatial and temporal image fusion model for complex land surface changes," *Remote Sens. Environ.*, vol. 208, pp. 42–62, 2018.
- [61] L. Huang, C. Zhao, C. Jiao, G. Zheng, and J. Zhu, "Quantitative analysis of rapid siltation and erosion caused coastline evolution in the coastal mudflat areas of Jiangsu," *Water*, vol. 15, no. 9, 2023, Art. no. 1679.
- [62] L. Mentaschi, M. I. Voudoukas, J. F. Pekel, E. Voukoulas, and L. Feyen, "Global long-term observations of coastal erosion and accretion," *Sci. Rep.*, vol. 8, no. 1, Aug. 2018, Art. no. 12876.
- [63] L. Zeng et al., "Sediment coarsening in tidal flats and stable coastline of the abandoned southern Yellow River sub-delta in response to fluvial sediment flux decrease during the past decades," *Front. Mar. Sci.*, vol. 8, 2021, Art. no. 761368.
- [64] D. Rayner, W. Glamore, L. Grandquist, J. Ruprecht, K. Waddington, and D. Khojasteh, "Intertidal wetland vegetation dynamics under rising sea levels," *Sci. Total Environ.*, vol. 766, Apr. 2021, Art. no. 144237.
- [65] R. Bishop-Taylor, S. Sagar, L. Lymburner, and R. J. Beaman, "Between the tides: Modelling the elevation of Australia's exposed intertidal zone at continental scale," *Estuarine, Coastal Shelf Sci.*, vol. 223, pp. 115–128, 2019.
- [66] Z. Zhou et al., "Processes, feedbacks, and morphodynamic evolution of tidal flat-marsh systems: Progress and challenges," *Water Sci. Eng.*, vol. 15, no. 2, pp. 89–102, 2022.
- [67] F. Xing, Y. P. Wang, and H. V. Wang, "Tidal hydrodynamics and fine-grained sediment transport on the radial sand ridge system in the southern Yellow Sea," *Mar. Geol.*, vol. 291–294, pp. 192–210, 2012.
- [68] X. Geng, H. A. Michael, M. C. Boufadel, F. J. Molz, F. Gerges, and K. Lee, "Heterogeneity affects intertidal flow topology in coastal beach aquifers," *Geophysical Res. Lett.*, vol. 47, no. 17, 2020, Art. no. e2020GL089612.
- [69] B. Zhao, Y. Liu, and L. Wang, "Evaluation of the stability of muddy coastline based on satellite imagery: A case study in the central coasts of Jiangsu, China," *Remote Sens.*, vol. 15, 2023, Art. no. 3323.
- [70] P. Borrelli et al., "An assessment of the global impact of 21st century land use change on soil erosion," *Nature Commun.*, vol. 8, no. 1, Dec. 2017, Art. no. 2013.



Yan Gu received the Ph.D. degree in marine geography from the School of Geography, Nanjing Normal University, Nanjing, China, in 2013.

She is currently an Associate Professor with the School of Geographic and Biologic Information, Nanjing University of Posts and Telecommunications, Nanjing, China. Her main research interests include remote sensing monitoring of coastal environment, UAV photogrammetry and 3-D modeling, and estuarine and coastal morphodynamics.



Jianchun Chen (Graduate Student Member, IEEE) received the bachelor's degree from the College of Disaster Prevention and Technology, China, in 2020. He is currently working toward the M.S. degree in surveying and mapping science and technology with the Nanjing University of Posts and Telecommunications, Nanjing, China.

His main research interests include remote sensing image processing, change detection, and multisource remote sensing data fusion.



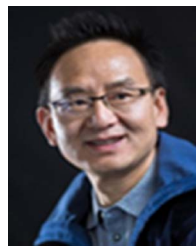
Shibing Zhu is currently working toward the Ph.D. degree in geography with Nanjing University, Nanjing, China.

His study primarily focuses on the geomorphology, hydrology, and sediment dynamics, with particular interest in coastal responses to global change and human activities.



Ziyao Chen received the bachelor's degree in geography and information systems from Anhui Normal University, Wuhu, China, in 2022. He is currently working toward the master's degree with the Nanjing University of Posts and Telecommunications, Nanjing, China.

The main research directions include remote sensing image processing and remote sensing cloud platform applications.



Ya Ping Wang received the Ph.D. degree in marine geology from the Institute of Oceanology, Chinese Academy of Sciences, Qingdao, China, in 2000.

He is currently a Professor with the School of Geography and Oceanography, Nanjing University, Nanjing, China, and the State Key Laboratory of Estuarine and Coastal Research, East China Normal University, Shanghai, China. His main research interests include marine sediment dynamics, benthic boundary layer processes, and estuarine and coastal morphodynamics.



Mingliang Li received the M.S. degree in marine geology from Nanjing University, Nanjing, China, in 2014.

He is currently a Geological Engineer with the Geological Survey of Jiangsu Province, Nanjing. His main research interests include coastal sediment dynamics and land–sea interactions.